Finite element model of training in the superconducting quadrupole magnet SQ02

Paolo Ferracin and Shlomo Caspi

Lawrence Berkeley National Laboratory, Berkeley, CA, USA

Abstract

This paper describes the use of 3D finite element models to study training in superconducting magnets. The simulations are used to examine coil displacements when the electromagnetic forces are cycled, and compute the frictional energy released during conductor motion with the resulting temperature rise. A computed training curve is then presented and discussed. The results from the numerical computations are compared with test results of the Nb_3Sn racetrack quadrupole magnet SQ02.

Keywords: Superconducting magnet, training, ratcheting

1. Introduction

High field superconducting magnets are susceptible to premature quenches. These quenches are caused by a sudden release of heat within the windings before the magnet reaches its critical limit. Possible sources of heating inside the coils arise either from magnetic instabilities, called flux jumps, or mechanical disturbances induced by electromagnetic forces [1-3]. These mechanical disturbances can be subdivided in two groups: conductor motions in the presence of friction and, in the case of an impregnated coil, fracturing of the epoxy [4,5].

When premature quenches persist during testing, the magnet is unable to reach the predicted operational limits, called “short sample limits”. Nevertheless, it has often been observed that mechanical disturbances may disappear after consecutive current ramps, and reappear only when the electromagnetic forces exceed the maximum level reached in the previous ramps. Under these circumstances (and with successive quenches), the magnet exhibits a continuous rise in its quench current; this phenomenon is generally described as training [6].

The training behavior exhibited by superconducting magnets can be qualitatively explained by irreversible changes in the coil’s mechanical status. For example, premature quenches produced by epoxy cracking take place when the stresses in the winding exceed the epoxy’s fracture stress. Once the epoxy is locally fractured, further cracking appears only when the Lorentz stress is increased. Furthermore, the non-reversible, microscopic sliding of conductors subjected to cycling loading (Kaiser effect), which has extensively been observed through measurements of acoustic emissions [7], can be reproduced by simple frictional models [8]. These analytical models indicate that, after each quench, the coil is partially locked by friction in a new and more secure state which allows the conductors to withstand higher levels of Lorentz forces. Other studies interpret training as the result of inelastic deformation of the coil during excitation, which progressively make the winding more rigid and thus less prone to move [9].

In past years, the Superconducting Magnet Group at LBNL has carried out several experimental and computational studies of the training phenomenon. Detailed analysis

has been performed on voltage signals recorded immediately before and after a quench, with the goal of determining the location of the quench and examining whether the quench is caused by flux-jumps or stick-slip mechanical motions [10]. At the same time, 3D finite element models have been implemented to study coil movement during excitation in order to better understand why quenches occur in particular locations [11].

In this paper, we describe a 3D finite element model aimed at evaluating the irreversible phenomena characterized as training from a quantitative point of view (early results of the analysis have been presented in [12]). The model investigates the progressive change in coil shape forced by consecutive current ramps and studies how the energy released by friction motions evolves with successive quenches. The computed frictional energy is then implemented as a heat source in a simplified 2D thermal model of the coil, and the resulting temperature rise is used to calculate a training curve.

The model was developed to study the performance of SQ02, a subscale racetrack quadrupole magnet recently fabricated and tested as part of the LARP Program [13]. In particular, the numerical analysis is aimed at understanding and reproducing three phenomena observed during testing: 1) the conductor-motion induced quenches in the pole turn, 2) the progressive increase of coil axial length after consecutive current ramps (ratcheting), and 3) the increase in quench current (training).

This paper begins with an overview of the design parameters and test results for SQ02, with an emphasis on quench performance and strain gauge measurements. The main features of the 3D finite element model and its assumptions are presented in Section 3. Finally, Section 4 describes the model results and compares them with measurements from the SQ02 test. The section concludes with a description of the training model and the final computation of the training curve.

2. Overview of the subscale quadrupole magnet SQ02

The U.S. LHC Accelerator Research Program (LARP), a collaboration between BNL, FNAL, LBNL, and SLAC, is developing Nb_3Sn accelerator magnet technology for the LHC luminosity upgrade. As part of the LARP Magnet Program, a series of Subscale Quadrupole (SQ) magnets, based on 300 mm long flat racetrack coils, has been built and

tested. In 2004, the first magnet SQ01 was fabricated and tested [14]. The second magnet of the series, SQ02, was tested in 2006.

2.1. Magnet design

The design of magnet SQ02 is based on four subscale coils arranged in a quadrupole configuration (Fig. 1a). Each coil is a double-layer flat racetrack, with 21 turns per layer wound around an aluminum bronze pole (island). The coil straight section is 152 mm long, while the total coil length is about 300 mm. The Rutherford cable, 7.793 wide and 1.276 mm thick, is composed of 20 Nb_3Sn strands with a diameter of 0.7 mm, and is insulated with a 0.1 mm thick woven sleeve of fiberglass. After winding, the coils are confined within a stainless steel horseshoe-end shoe containment structure, reacted, epoxy impregnated, and placed around a square aluminum bore. The bore has a clear round aperture of 110 mm. The coil-bore sub-assembly is then surrounded by four stainless steel pads and inserted into a structure composed of a four-piece iron yoke and an aluminum shell (Fig. 1b). Within a 5 mm gap between the pads and yokes, four water-pressurized bladders are used to apply tension to the shell and pre-compress the coil-pads subassembly. Once the structure is locked with eight interference keys, the bladders are deflated and removed. A longitudinal support system is also included in the design: four aluminum rods, with a diameter of 25 mm, are inserted into four holes in the pads, and bolted to two 50 mm thick stainless steel end plates that rest against the coil end-shoes (Fig. 2a). The rods are pre-tensioned with an axial piston at room temperature. During cool-down, both the shell and the rods increase their tension, due to the higher thermal contraction of the aluminum.

The magnet current limit (or short sample current I_{ss}) was determined from the intersection between the critical curves measured on strands extracted from the cable and the computed magnet load line [15]. The magnet expected short sample current at 4.3 K is 9.9 kA. The magnetic field in the conductor reaches its peak value of 11.1 T in the pole turn end region (close to the tip of the island) and decreases to 9.7 T in the straight section (Fig. 2b). The main component of the Lorenz force in the straight section F_{ss} (sum of the forces acting on all the conductors in the straight section) is 176 kN and, as shown in Fig. 1a, tends to separate the coil blocks from the island, pushing them towards the

magnetic mid-plane. In the longitudinal direction, because of the high energy stored in the magnet (142 kJ), a significant axial force F_z of 83 kN (obtained by the vector sum of the entire axial force acting on each coil end) pushes each coil outwardly. In order to minimize conductor movement during excitation, the coil is pre-stressed by the structure in all directions. After cool-down, the measured shell tension increases to 105 MPa, corresponding to a computed coil pre-compression of 85 MPa along the straight section. The rods reach a measured tension of 125 MPa, which translates to a total axial load on the magnet ends of about 270 kN. The coil instrumentation includes 8 voltage taps (4 per layer) on the innermost cable around the island (pole turn), where the highest field was expected. These taps subdivide the pole turn into straight segments and end segments, thus measuring the quench location as well as its propagation velocity.

2.2. Test results of SQ02

2.2.1. Quench performance

The test of SQ02 included two thermal cycles at 4.3 K (we refer to [16] for a complete description of the test results). The first magnet quench occured at 5.9 kA (60% of I_{ss}), and reached a plateau of 9.5 kA (97% of I_{ss}) in the second thermal cycle. As shown in Fig. 3, during the first 13 quenches the magnet rapidly reached about 90% of I_{ss}, with an increase of 200 A to 400 A between consecutive quenches. The quench current increased at a significantly lower rate in subsequent current ramps.

Quench locations and propagation velocities were investigated through the “time of flight” technique: all of the training quenches were located in the innermost turn around the island (pole turn), where the highest field was expected (see blue markers in Fig. 4). Moreover, the analysis of the voltage taps data indicated that the training quenches originated in the end region, and progressively moved towards the center of the straight section (as pointed out by the arrows in Fig. 4). As the magnet reached its maximum current, all the quench locations reversed back to the end region (close to the tip of the island), where the coil peak field is located (see red markers in Fig. 4). The voltage-spikes recorded before each quench indicated that all training quenches were preceded by mechanical motions (“slip-stick” quench onset), while the quenches at the end of the

plateau were characterized by the exhausted-margin quench onset signature, typical of short sample quenches [10].

2.2.2. Strain gauge measurements

The axial aluminum rods were instrumented with strain gauges. Since the rods were in direct contact with the coil ends (via end plates), any coil axial displacement induced by the *z* component of the electromagnetic forces resulted in a change in rod strain. During the first 13 quenches, when most of the magnet training occurred, the rod strain showed a progressive and continuous change of coil shape. In Fig. 5, the incremental increase in rod strain (and coil length) is plotted as a function of the fraction of Lorentz force with respect to the 4.3 K short sample value $[(I/I_{ss})^2]$. As explained in the previous sections, the axial component of the Lorentz force tends to pull the coil-end outwardly. As a result, the coils, as well as the rods, are elongated along the *z* direction. During the first current ramp, prior to the first quench, the rods stretched 15 μstrain, indicating that the coil underwent a total elongation of about 4 μm. After the quench, when the current decreased to zero and the Lorentz force vanished, the rods maintained a residual strain (about 3 μstrain), showing that the coil remained partially elongated. During subsequent training ramps, as the quench current reached higher levels, the total residual strain increased as well, indicating that the larger the force, the greater the coil lengthening (Fig. 6). This phenomenon, called ratcheting, has been observed in previous magnets [17-20], and can be related to the friction between the coil and its surrounding components. After each excitation ramp, friction partially locks the coil in its deformed state, preventing the conductor from returning to its original pre-load state.

3. 3D finite element magneto-mechanical model

A complete 3D finite element model of SQ02 has been used to study and interpret the test results described in Section 2. The model required the integration of two computer programs: ANSYS was used for the mechanical and thermal analysis, whereas OPERA 3D was used for the magnetic analysis. An ANSYS input file was executed to create the solid volumes and assign material properties and meshing requirements (Fig. 7). The coil was simulated as a single block of conductors, with uniform and linear material

properties. Elements were generated using a volume sweep of 20-node structural element (SOLID95). The entire conductor/structure loading process was simulated using the following four steps. 1) Bladder pre-stressing: a uniform pressure was applied to all bladder-contact areas of the pads and yokes. The keys were “turned off”, allowing them to respond to geometric changes, but preventing them from transmitting forces. 2) Keying: the interference keys were “turned on”, and the bladder pressure deleted, using the ANSYS “alive” operation. 3) Cool-down to 4.3 K: the temperature of all solids was changed from 300 K to 4.3 K. 4) Magnetic excitation: the Lorentz forces were transferred from an OPERA 3D model to each coil element in the mechanical model.

The assembly components in the mechanical model were not bonded, but they were allowed to interact via contact elements (TARGE170 and CONTA174) along adjacent surfaces (see Fig. 8 for the details of the coil-island contact region). For all the contact surfaces between the coil block and the surrounding components (in particular the island), both frictionless and frictional sliding has been considered, with a static friction factor μ ranging from 0.25 to 0.75.

4. Model results

4.1. Conductor motion

Since all the training quenches were located in the pole turn and were immediately preceded by a “slip-stick” voltage spike, we tested whether or not the mechanical model could reproduce the conductor motion in the proximity of the contact region between coil and island.

As a first step, to perform a preliminary model validation and tune the friction factors, we compared the measured rod response during excitation with the model predictions. As shown in Fig. 9, if frictionless contact is assumed between the components, the numerical computations significantly overestimate the coil elongation during excitation. Once a friction factor of 0.25 is included in the model, the coil motion during excitation is reduced, and the computed rod strain variation, although still slightly higher, becomes more consistent with the measurements. Increasing the friction factor up to a value of 0.75 does not significantly improve the results. As a possible explanation for the

remaining discrepancy between model and measurements, we point out that the island is epoxy-impregnated with the coil; as a result, the contact surface between pole turn and island is characterized by a bonding strength, which reduces to zero once the epoxy fractures. By allowing separation between components, the model simulates an "upper bound" situation with respect to the real conditions of a potted coil. A possible alternative, consisting in gluing the coil to the island only up to a certain stress level has been recently reported [21]. Throughout this paper, we will assume that the coil is allowed to separate and slide with respect to the island, with a friction factor of 0.50. In Section 4.4, we will show how, with this friction coefficient, the model seems to better reproduce the observed magnet quench performance.

If we look in more detail at the simulations of the coil behavior during excitation, we notice that the model predicts a clear change in coil shape as the current is ramped. In Fig. 10 we show the shape of the deformed coil, where the displacements are enhanced by a factor 70. The computation indicates that when the magnet is energized, the axial component of the Lorentz force tends to stretch the coil in the longitudinal direction. The resulting coil elongation (or strain) in the *z* direction produces a combined effect along the contact surface between the pole turn and the island: a separation (gap) in the end region, and a relative motion in the straight section (sliding). In Fig. 11 we plotted the computed gaps and sliding distance on a path along the coil-island contact region, centered in the transition between the end and the straight section: the predicted end gap, negative in sign, increases to 0.08 mm at 10 kA, whereas the relative sliding of the conductor region still in contact, positive in sign, propagates into the straight section.

To evaluate the importance of pre-stress and friction on the pole turn gap/sliding, we performed the computation with different degrees of shell and rod tension after cool-down and modified friction factors. When the axial rod tension after cool-down is reduced from 125 MPa to 85 MPa, and the shell tension is maintained at the nominal level of 105 MPa, the coil-island gap at the tip of the island increases from 0.08 mm to 0.09 mm, while no significant variation is observed in the straight section sliding (Fig. 12a). On the other hand, a reduction of the shell tension from 105 MPa to 80 MPa and a constant nominal rod tension of 125 MPa, resulted in a lower coil pre-stress in the straight section (from 85 MPa to 70 MPa), and consequently an increase in pole turn

sliding. If we vary the friction factor between the coil and the surrounding components (Fig. 12b), we noticed that both the sliding, its penetration in the straight section, and the end gap all increase when the friction is reduced. We can therefore conclude that, according to the 3D mechanical model, both coil pre-stress and friction between components play a major role in limiting conductor motions during magnet excitation.

4.2. Dissipated frictional energies

Since one of the goals of the analysis is to interpret and understand the quench occurrence at the pole turn during the SQ02 test, a fundamental parameter to be investigated is the energy released during conductor movement. Whenever two surfaces slide with respect to each other in a frictional environment, frictional energy is dissipated. The frictional energy dissipated per unit area E (J/m^2) can be estimated as

$$E = \delta \, \sigma_{f:} \tag{1}$$

where δ (m) is the relative sliding of the pole turn with respect to the island, and $\sigma_{f:}$ (N/m^2) is the frictional stress between the two surfaces (in the direction parallel to the two surfaces). When sliding occurs, the frictional stress can be express as

$$\sigma_{f:} = \mu \, P \tag{2}$$

where μ is the friction factor, and P (N/m^2) is the contact pressure between the two surfaces. It is important to point out that, when separation occurs (see end regions in Fig. 10), the contact pressure P is zero, and therefore the model does not predict any energy dissipated by a conductor motion. We computed the frictional energy dissipated at the coil-island interface during excitation at different currents and plotted the results along the transition between the end region and the straight section (Fig. 13). Between 0 kA to 3 kA, the release of frictional energy near the end peaks at about 57 J/m^2. During the following current ramps, the peak dissipated energy progressively increased to a maximum of 160 J/m^2 from 9 kA to 10 kA, and its location gradually moved towards the straight section. Therefore, in agreement with observations during magnet testing, the model predicts a quench-triggered displacement in the pole turn, with a consequent dissipation of energy whose peak location moved from the end to the straight section as the current increases. Moreover, as expected, the total frictional energy dissipated during excitation varied linearly with the Lorentz force, i.e. quadratically with the current, and

strongly depends on the friction factors (Fig. 14). As done in the previous section, we evaluated the effect of initial pre-stress and friction on the dissipated energy (Fig. 15a and 15b): when the shell tension or the friction is reduced, the profile of frictional energy is characterized by a smaller peak but a larger penetration into the straight section.

4.3. Ratcheting and irreversible energy release

The second phenomenon analyzed with the finite element model is ratcheting, the residual elongation experienced by the coil after each ramp. The analysis includes two different computations. In the first computation, we increased the Lorentz forces continuously ("ramp-up" case) up to about 9 kA. In the second computation ("cycles" case), we firstly introduced a load cycle where the force is initially raised up to 6 kA and abruptly removed. Then, in a second cycle, we reapplied the Lorentz force, first to its previous value of 6 kA and then to a new higher current (6.5 kA). We repeated this loading-unloading process increasing the current in steps of 500 A up to 9 kA. As shown in Fig. 16, when friction is included and loads are cycled, the simulation becomes non-conservative, and the results become path-dependent. This means that the computed rod strain under zero Lorentz force is now continuously changing (ratcheting) with respect to previous load cycles. This continuous change in coil length can be explained as follows: as the Lorentz forces are applied during the first loading cycle, a certain number of contact elements start sliding in the transition-straight section zone (Fig. 11). In this phase, the resulting friction force of the sliding contact elements opposes the motion, i.e. it has the opposite sign with respect to the Lorentz force. When the Lorentz forces are removed, the friction force reverses direction, maintaining the coil partially elongated. When, in the second cycle, the same Lorentz forces are re-applied, the coil returns to its previous deformed state. Then, when the current is further increased ("virgin territory"), new sliding takes place a larger number of contact elements (along the straight section) (Fig. 11). As a consequence, the resulting frictional force is larger than during the first cycle, and the coil residual elongation is increased when the electromagnetic forces are removed.

The same path-dependent behavior can be calculated for the frictional energy (Fig. 17). Consider the coil sliding during the "ramp-up" phase: the maximum energy released

between 6.5 kA – 7.0 kA is about 57 J/m^2. Assuming that a quench occurs at 7.0 kA, we first remove the force, and then we ramp again from 0 kA to 7.0 kA. The energy dissipated during the second ramp (0 - 7.0 kA) is negligible (at most 3 J/m^2). When the current is further increased from 7.0 kA – 7.5 kA, the coil tracks the original "ramp-up" curve again, and the energy reaches a peak of 58 J/m^2. The same behavior characterizes the subsequent loading-unloading cycles. We can therefore conclude that after a quench, the frictional model predicts a new state of deformation for the coil, which minimizes the dissipated energy until the coil experiences a new level of forces (virgin territory).

4.4. Training

As a final step in the analysis, we transfer the numerical results obtained from the 3D finite element model to a simplified 2D thermal model, with the goal of obtaining a training curve. A cross-section of the 2D thermal model is shown in Fig. 18. The model simulates a portion of the coil composed by two strands, the cable-island insulation, and the aluminum-bronze island (Fig. 18a). Adiabatic conditions are imposed along the boundaries of the model. The strand model includes the superconductor, the copper matrix, and the epoxy (Fig. 18b). The frictional energy (J/m^2) computed by the 3D mechanical model is inputted into the thermal model as a pulse of heat generation (J/m^3/s) of 1 ms (typical duration of a motion induced quench triggering event, according to [1]), applied to the insulation between strands and island (Fig. 18c). As an output, the model provides the peak temperature in the superconductor as a function of the frictional energy (Fig. 19a). As a first step of the analysis, we assume that a quench occurs when the temperature of current sharing T_{cs} is reached in any location of the superconductor.

Now, in Fig. 14 we showed how the total maximum frictional energy accumulates during a ramp and varies as a function of current. Under the assumption that all the frictional energy accumulated during a ramp is released in 1 ms, we can now plot the peak temperature of the superconductor as a function of current (Fig. 19b). The resulting temperature rise in the superconductor can then be compared with the available temperature margin. The results are plotted in Fig. 20, where for each ramp we show the computed rod response in strain, the superconductor temperature rise, and the temperature margin. For example, during the first current ramp (Fig. 20a and 20b),

negligible energy is dissipated up to 2 kA. Beyond 2 kA, frictional energy starts to be dissipated. When we reach a current of 5.6 kA, assuming that all the accumulated frictional energy is dissipated in 1 ms, the peak temperature of the superconductor is increased to 11.3 K, corresponding to temperature of current sharing at that level of current and field. In these conditions, the first quench is assumed, and the current is reduced to zero. In the second ramp, because of the ratcheting effect described in the previous section, we can assume that a negligible amount of energy is dissipated up to 5.6 kA (Fig. 20c and 20d). Then, the model predicts that the conductor current sharing temperature is reached at a current of 6.6 kA. By repeating this computation with increasing currents, and decreasing temperature margin, a training curve can be generated (Fig. 21). The computed curve is consistent with the training observed in SQ02. As mentioned early, a friction factor of 0.50 seems to better reproduce the test results, with a slight underestimation of the first quench current, but a faster quench current increase in the following ramps.

5. Conclusions and perspectives

The analysis described in this paper shows that it is possible to calculate non-reversible processes, such as ratcheting and training, observed in the superconducting quadrupole magnet SQ02. By combining a 3D mechanical model with a 2D thermal model, we were able to explain the quench locations recorded by voltage taps, to reproduce the change in coil shape measured by strain gauges, and to generate a series of consecutive quenches consistent with test results.

The computed training curve is strongly dependent on the value of the friction coefficient, coil pre-stress, and time of frictional energy release. As a next step, the 3D model will be modified in order to better reproduce the coil-island interface by assuming a certain bonding strength between the contact elements. Moreover, a refinement of the thermal model will include the analysis of Minimum Quench Energies [22] and Minumum Propagation Zones [23] as parameters to determine when and where a quench is expected to occur.

Another parameter which can affect the results of the mechanical model is the elastic modulus of the superconducting coil. Measurements performed on stacks of conductors

have shown that coils feature strong nonlinear stress-strain behavior characterized by hysteresis phenomena [24]. An upgraded version of the finite element code should include a more realistic modeling of the coil rigidity, and investigate its impact on the progressive change in coil shape during current ramps.

At this stage of the work, it is already possible to use the model and the computed training curve as a tool to compare different support structures or pre-stress conditions, and investigate the optimum way to mechanically confine a superconducting coil in order to improve quench performance.

6. Acknowledgements

We would like to acknowledge A.F. Lietzke and S.O. Prestemon for stimulating discussion about magnet training and friction effects. This work was supported by the Director, Office of Energy Research, Office of High Energy and Nuclear Physics, High Energy Physics Division, U. S. Department of Energy, under Contract No. DE-AC02-05CH11231.

7. References

[1] Wilson MN. Superconducting magnets. Oxford: Clarendon Press, 1983.

[2] Wipf SL. Stability and degradation of superconducting current-carrying devices. Los Alamos Report, LA 7275, 1978.

[3] Devred A. Quench origins. AIP Conf Proc 1992;249:1263.

[4] Iwasa Y. Mechanical disturbances in superconducting magnet – A review. IEEE Trans Magn 1992;28(1):113.

[5] Iwasa Y. Experimental and theoretical investigation of mechanical disturbances in epoxy-impregnated superconducting coils. 1. General introduction. Cryogenics 1985;25(6):304.

[6] Brechna H, Turowski P. Training and degradation phenomena in superconducting magnets. Proceedings of the 6th International Conference on Magnet Technology, 1978. p. 597.

[7] Maeda H, Tsukamoto O, Iwasa Y. The mechanism of frictional motion and its effect at 4.3 K in superconducting magnet winding models. Cryogenics 1982;22(6):287.

[8] Tsukamoto O, Iwasa Y. Sources of acoustic emissions in superconducting magnets. J Appl Phys 1983;54(2):997.

[9] Keilin VE. Explanation of main features of superconducting windings training by balance of acting and permissible disturbances. IEEE Tran Appl Supercond 1983;3(1):297.

[10] Lietzke AF, et al. Differentiation of performance-limiting voltage transients during Nb_3Sn magnet testing. AIP Conf Proc 2006;824:550.

[11] Caspi S, et al, Towards integrated design and modeling of high field accelerator magnets. IEEE Trans Appl Supercond 2006;16(2):1298.

[12] Gourlay SA, et al. Magnet R&D for the US LHC Accelerator Research Program. IEEE Trans Appl Supercond 2006;16(2):324.

[13] Ferracin P, et al. Towards Computing Ratcheting and Training in Superconducting Magnets. Presented at Applied Superconductivity Conference 2006.

[14] Ferracin P, et al. Development of a large aperture Nb_3Sn racetrack quadrupole magnet. IEEE Trans Appl Supercond 2005;15(2):1132.

[15] Barzi E, et al. Round and extracted Nb_3Sn strand tests for LARP magnet R&D. IEEE Trans Appl Supercond 2006;16(2):319.

[16] Ferracin P, et al. Assembly and test of SQ02, a Nb_3Sn racetrack quadrupole magnet for LARP. Presented at Applied Superconductivity Conference 2006.

[17] Strait J, et al. Tests of full scale SSC R&D dipole magnets. IEEE Trans Magn 1989;25(2):1455.

[18] Buckley J, et al. Mechanical performance of a twin-aperture 56 mm bore 1 m long dipole model made with SSC type cables. IEEE Trans Magn 1996;32(4):2136.

[19] Devred A, et al. About the mechanics of SSC dipole magnet prototypes. AIP Conf Proc 1992;249:1309.

[20] Mattafirri S, et al. Performance analysis of HD1: a 16 T Nb_3Sn dipole magnet. IEEE Trans Appl Supercond 2005;15(2):1156.

[21] Wands B. Magneto-structural analysis of the Fermilab TQC Nb_3Sn high gradient quadrupole end region. Presented at the CHATS-AS Workshop 2006.

[22] Wilson MN and Wolf R. Calculation of minimum quench energies for Rutherford cables. IEEE Trans Appl Supercond 1997;7(2):950.

[23] Wipf SL and Martinell AP. Investigation of cryogenic stability and reliability of operation of Nb_3Sn coils in Helium gas environment. Proceeding of Applied Superconductivity Conference 1972, p.331.

[24] Chichili DR, et al. Investigation of cable insulation and thermo-mechanical properties of epoxy impregnated Nb_3Sn composite. IEEE Trans Appl Supercond 2000;10(1):1317.

Figures

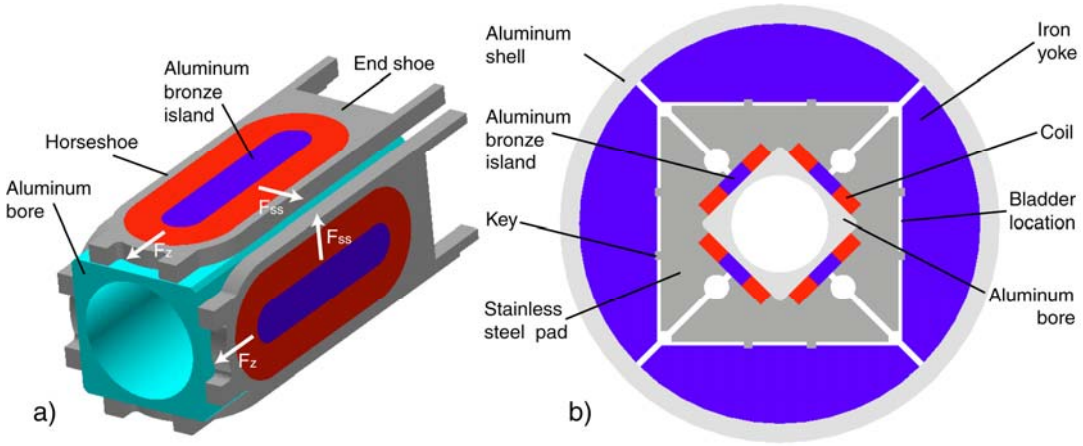

Fig. 1. a) SQ02 coil configuration and Lorentz force directions. b) Magnet cross-section.

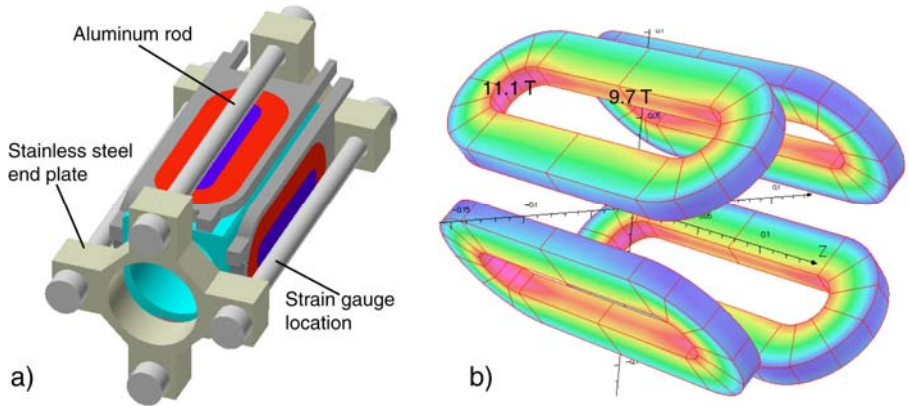

Fig. 2. a) SQ02 axial support. b) Magnetic field in the coil.

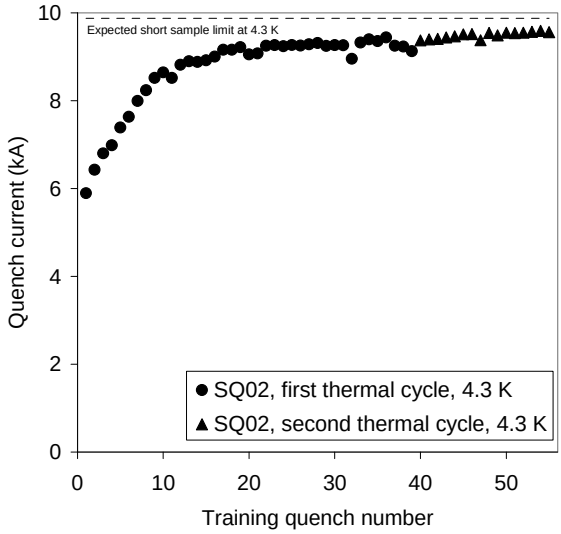

Fig. 3. Training performance of SQ02 at 4.3 K (two thermal cycles). The dashed line represents the expected current limit based on short sample measurements.

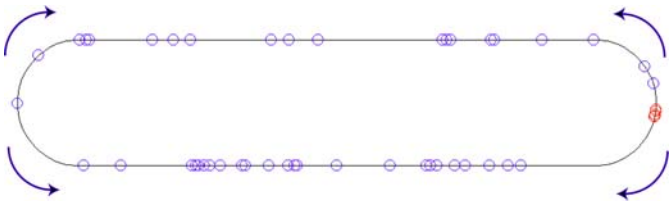

Fig. 4. Quench locations in the pole turn during the two thermal cycles: training quenches (blue markers), and plateau quenches (red markers). Both pole turns (inner and outer layer) are projected on the same plane. We refer to [16] for the detailed analysis of the quench locations.

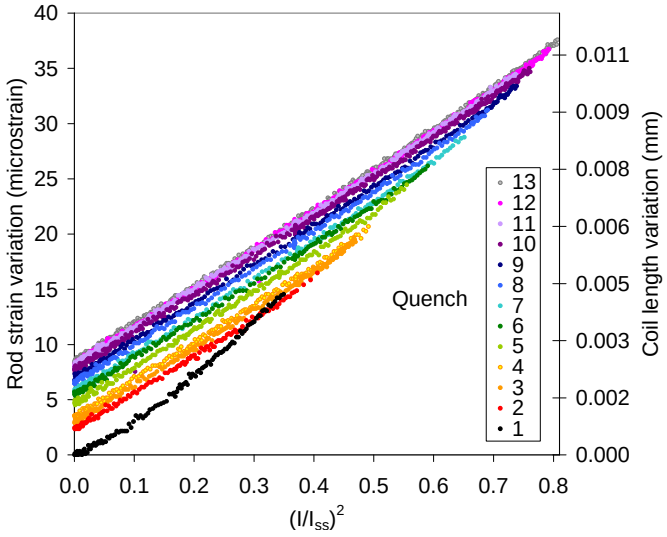

Fig. 5. Measured variation of rod strain (left axis) and coil length (right axis) as a function of the fraction of Lorentz force with respect to the 4.3 K short sample value. The first 13 ramps of training are shown.

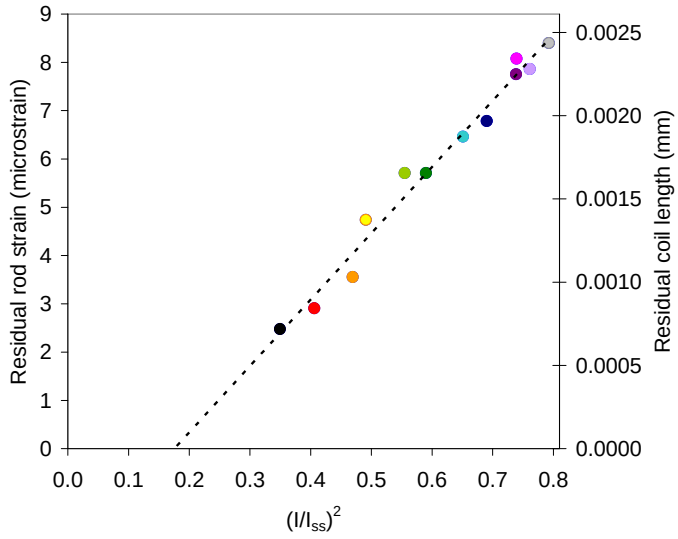

Fig. 6. Measured residual rod strain (left axis) and coil elongation (right axis) as a function of the fraction of Lorentz force with respect to the 4.3 K short sample value reached during an excitation cycle.

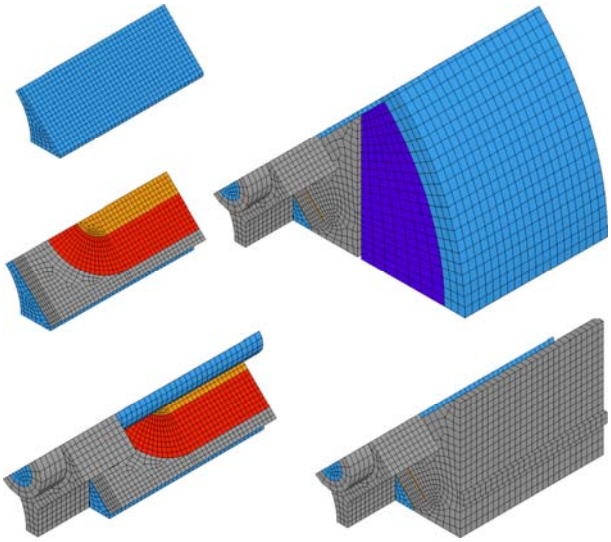

Fig. 7. 3D finite element mechanical model of SQ02.

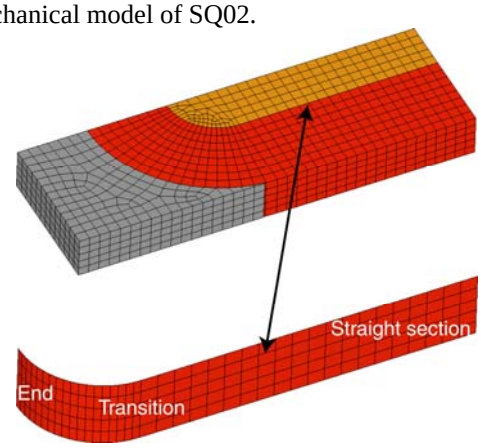

Fig. 8. Contact elements between coil and island.

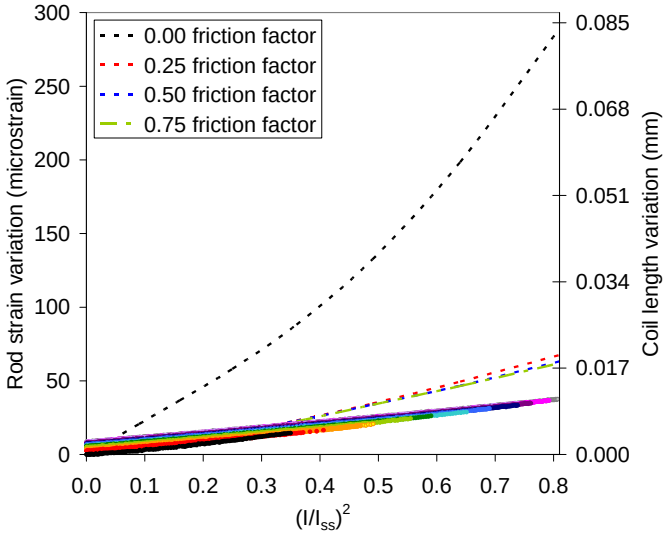

Fig. 9. Comparison between measured (colored markers, see Fig. 5) and computed (dashed lines) variation of rod strain (left axis) and coil length (right axis) as a function of the fraction of Lorentz force with respect to the 4.3 K short sample value.

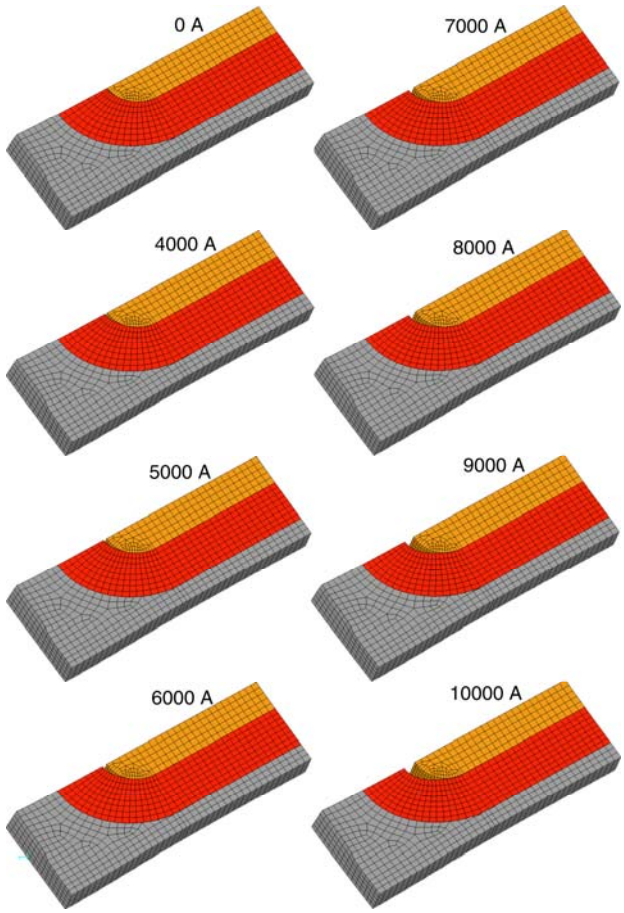

Fig. 10. Coil deformed shape as a function of current (displacements are enhanced by a factor 70).

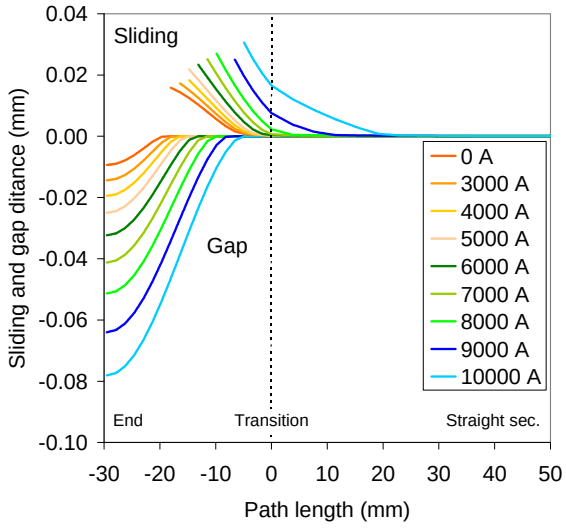

Fig. 11. Computed sliding distance (positive) and gap distance (negative) between coil and island at different currents: data are plotted along a path from the center of the straight section to the end section (see contact elements in Fig. 8). A friction factor of 0.50 between coil and island is assumed. The sliding distance is plotted only for the region where island and pole turn are still in contact.

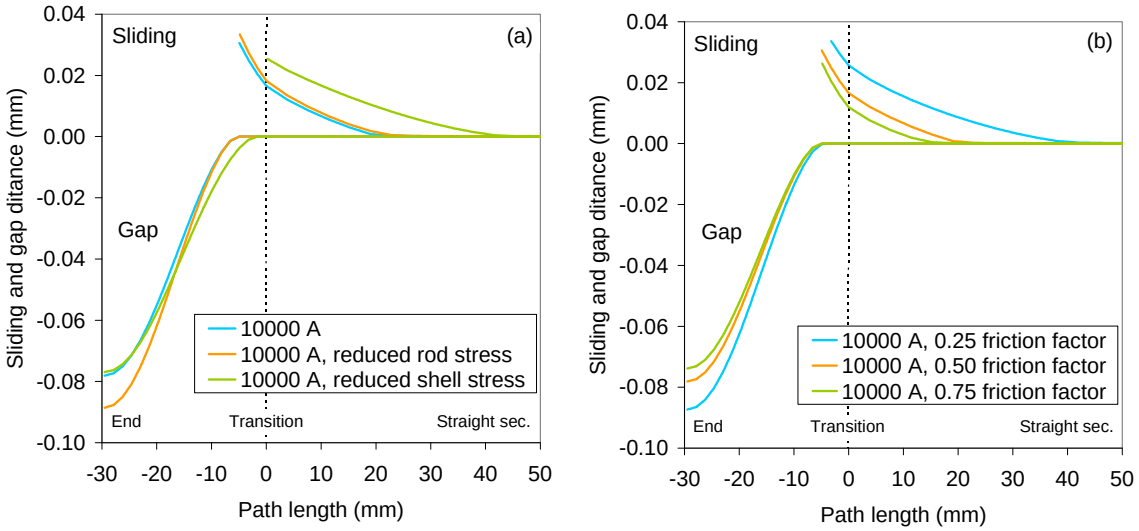

Fig. 12. Computed sliding distance (positive) and gap distance (negative) between coil and island: data are plotted along a path from the center of the straight section to the end section (see contact elements in Fig. 8). a) In the "reduced rod stress" case, the axial rod tension after cool-down is reduced from 125 MPa to 85 MPa, and the shell tension is maintained at the nominal level of 105 MPa, while in the "reduced shell stress" case, the shell tension after cool-down is reduced from 105 MPa to 80 MPa, with the rod tension kept at the nominal level of 125 MPa. A friction factor of 0.50 between coil and island is assumed. b) Effect of different friction factors.

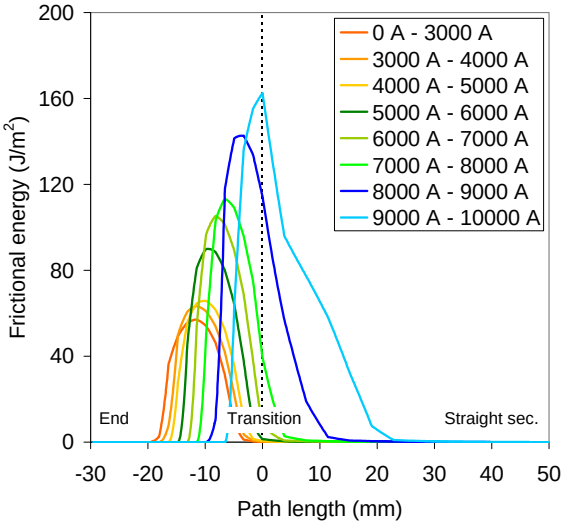

Fig. 13. Computed frictional energy (J/m^2) dissipated between coil and island at different current ranges: data are plotted along a path from the center of the straight section to the end section (see contact elements in Fig. 8). A friction factor of 0.50 between coil and island is assumed.

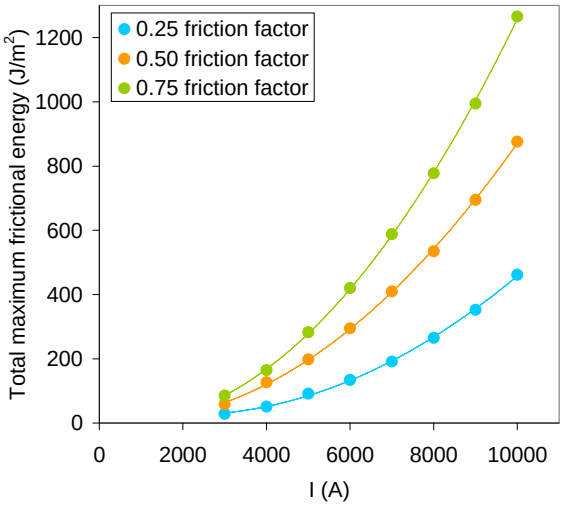

Fig. 14. Total maximum frictional energy dissipated as a function of current and of the friction factor between coil and island.

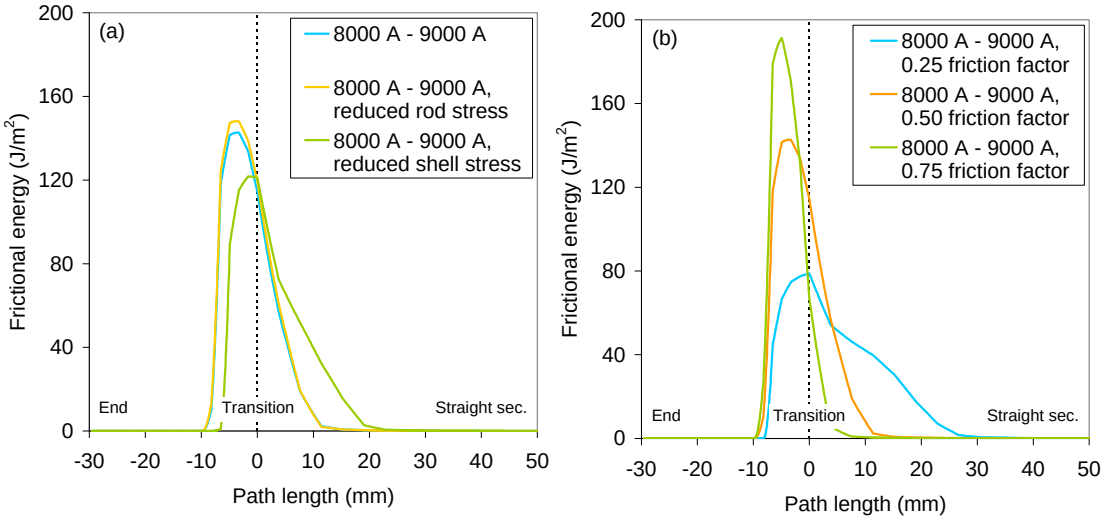

Fig. 15. Computed frictional energy (J/m^2) dissipated between coil and island at different current ranges: data are plotted along a path from the center of the straight section to the end section (see contact elements in Fig. 8). a) In the "reduced rod stress" case, the axial rod tension after cool-down is reduced from 125 MPa to 85 MPa, and the shell tension is maintained at the nominal level of 105 MPa, while in the "reduced shell stress" case, the shell tension after cool-down is reduced from 105 MPa to 80 MPa, with the rod tension kept at the nominal level of 125 MPa. A friction factor of 0.50 between coil and island is assumed. b) Effect of different friction factors.

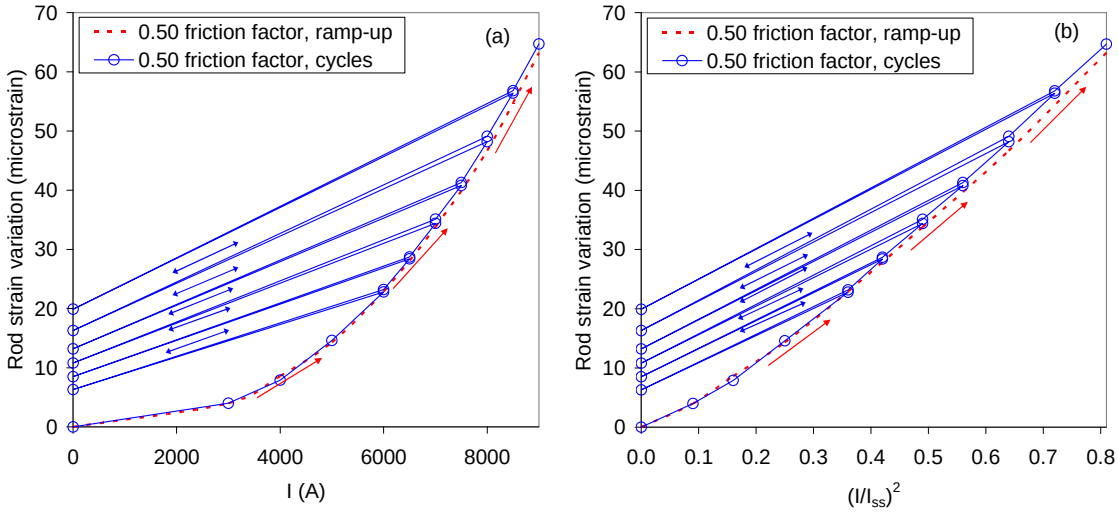

Fig. 16. Computed variation of rod strain as a function of current (a) and of the fraction of Lorentz force with respect to the 4.3 K short sample value (b).

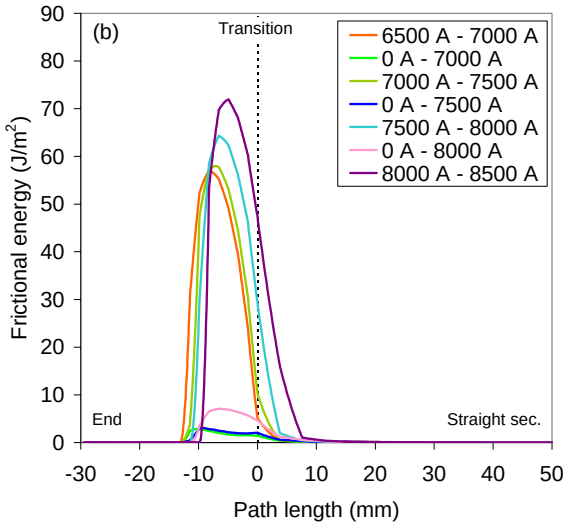

Fig. 17. Computed frictional energy in consecutive loading-unloading cycles: data are plotted along a path from the center of the straight section to the end section (see contact elements in Fig. 8). A friction factor of 0.50 between coil and island is assumed.

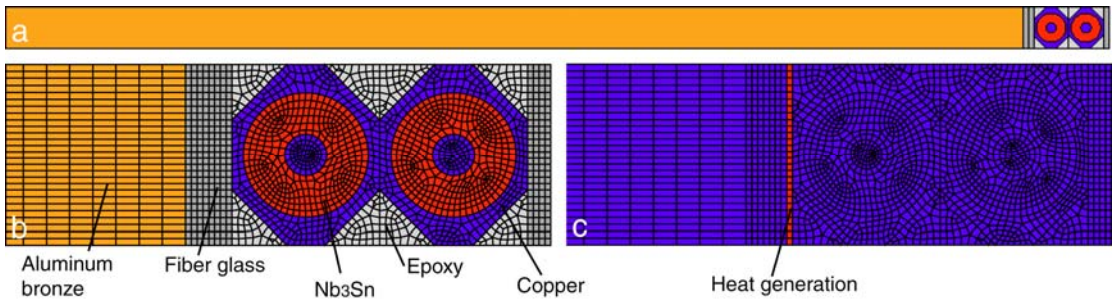

Fig. 18. 2D thermal model. a) Complete cross-section. b) Details of the strand mesh. c) Details of the region where the frictional energy computed by the 3D mechanical model is released.

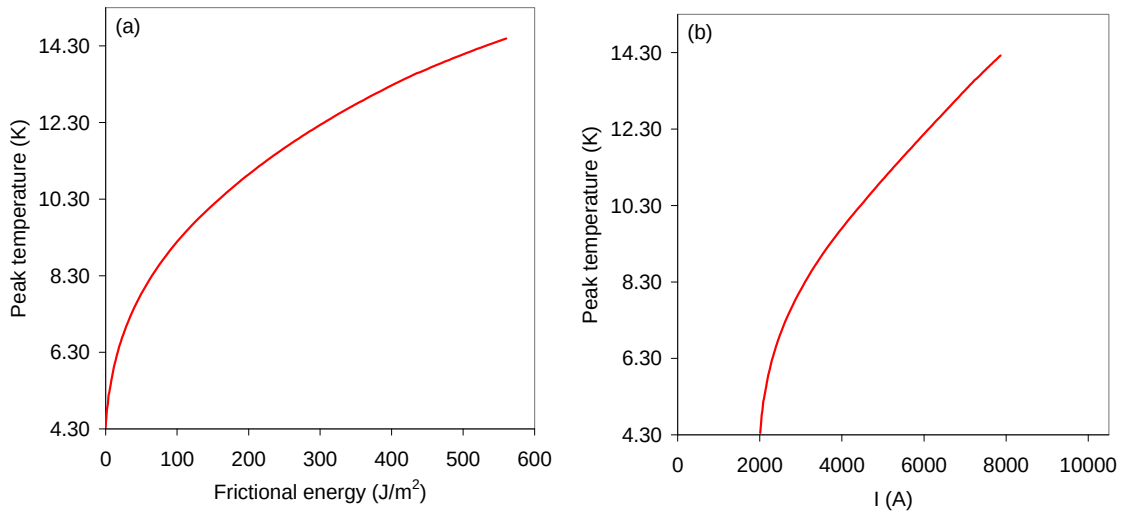

Fig. 19. Computed peak temperature as a function of the frictional energy and of the correspondent current.

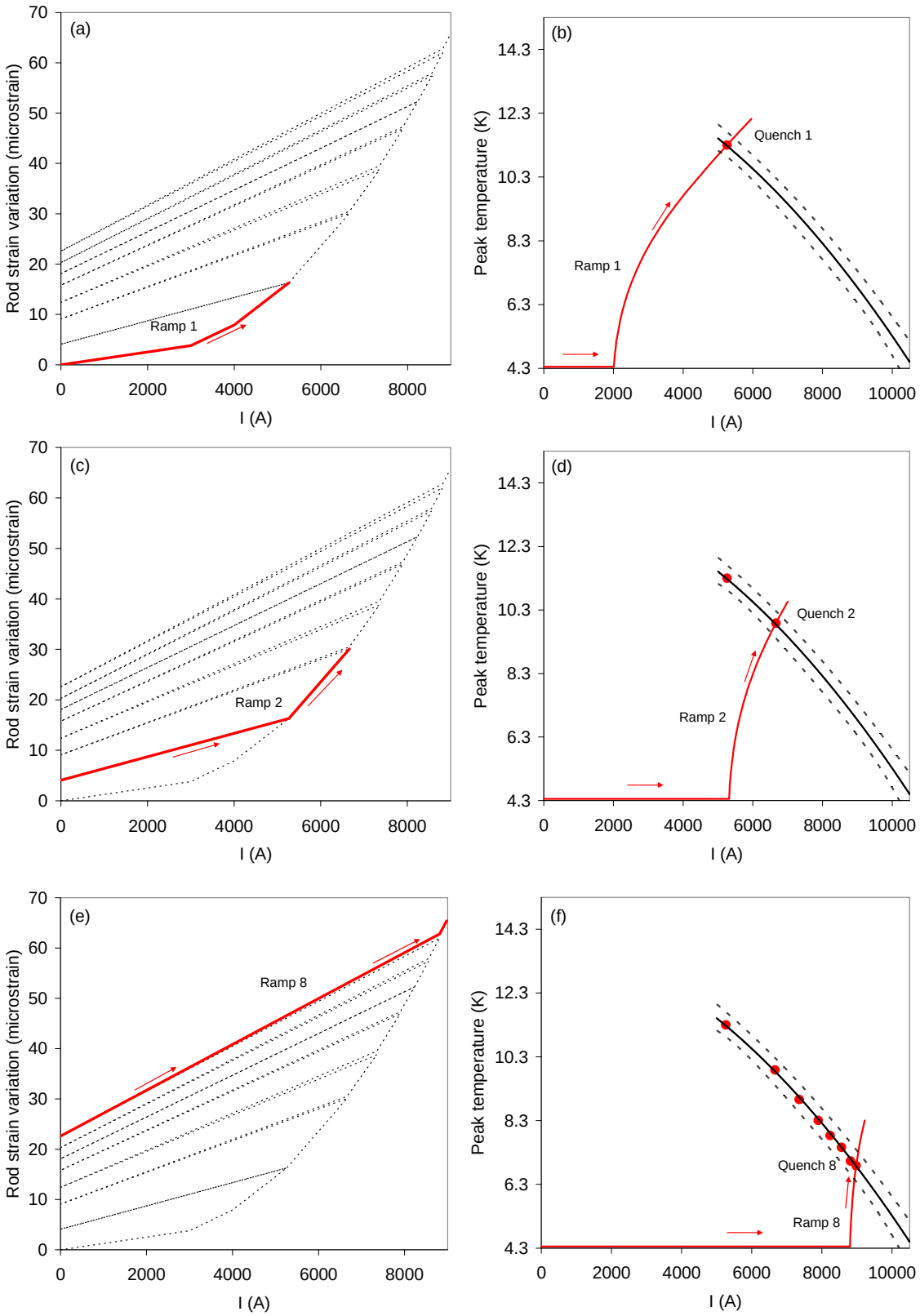
(a)
Rod strain variation (microstrain)
I (A)
Ramp 1
(b)
Peak temperature (K)
I (A)
Quench 1
Ramp 1
(c)
Rod strain variation (microstrain)
I (A)
Ramp 2
(d)
Peak temperature (K)
I (A)
Quench 2
Ramp 2
(e)
Rod strain variation (microstrain)
I (A)
Ramp 8
(f)
Peak temperature (K)
I (A)
Quench 8
Ramp 8

Fig. 20. Left: computed variation of rod strain as a function of current during consecutive current ramps. Right: peak temperature of the superconductor induced by frictional energy computed during consecutive current ramps (solid red lines) and temperature of current sharing vs. current (black line).

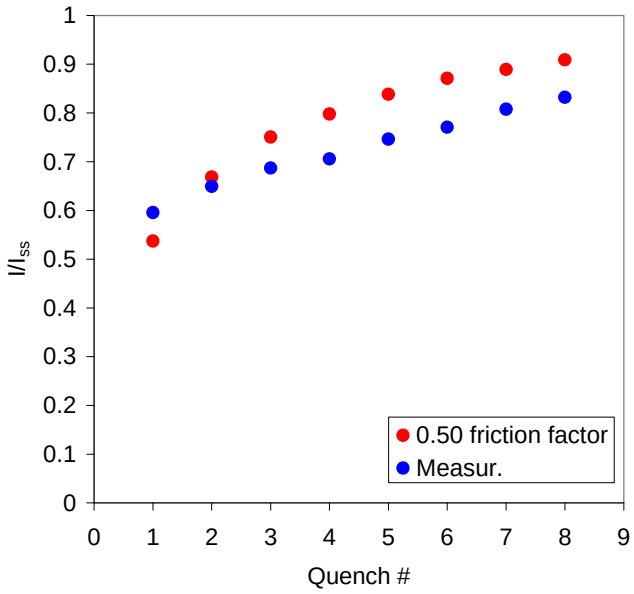

Fig. 21. Computed and measured training curve.